A Scalable Partitioned Approach to Model Massive Nonstationary Non-Gaussian Spatial Datasets

Benjamin Seiyon Lee and Jaewoo Park*

Department of Statistics, George Mason University

Department of Statistics and Data Science, Yonsei University

Department of Applied Statistics, Yonsei University

November 30, 2020

Abstract

Nonstationary non-Gaussian spatial data are common in many disciplines, including climate science, ecology, epidemiology, and social sciences. Examples include count data on disease incidence and binary satellite data on cloud mask (cloud/no-cloud). Modeling such datasets as stationary spatial processes can be unrealistic since they are collected over large heterogeneous domains (i.e., spatial behavior differs across subregions). Although several approaches have been developed for nonstationary spatial models, these have focused primarily on Gaussian responses. In addition, fitting nonstationary models for large non-Gaussian datasets is computationally prohibitive. To address these challenges, we propose a scalable algorithm for modeling such data by leveraging parallel computing in modern high-performance computing systems. We partition the spatial domain into disjoint subregions and fit locally nonstationary models using a carefully curated set of spatial basis functions. Then, we combine the local processes using a novel neighbor-based weighting scheme. Our approach scales well to massive datasets (e.g., 1 million samples) and can be implemented in `nimble`, a popular software environment for Bayesian hierarchical modeling. We demonstrate our method to simulated examples and two large real-world datasets pertaining to infectious diseases and remote sensing.

Keywords: Markov chain Monte Carlo, spatial partition, basis representation, parallel computing, nonstationary process, non-Gaussian spatial data

---

*Corresponding Author: Department of Statistics and Data Science, Yonsei University; Department of Applied Statistics, Yonsei University, Seoul, 03722, Republic of Korea (e-mail: jwpark88@yonsei.ac.kr)

1 Introduction

Nonstationary spatial models have been used in a wide range of scientific applications, including disease modeling (Ejigu et al., 2020), remote sensing (Heaton et al., 2017), precision agriculture (Katzfuss, 2013), precipitation modeling (Risser and Calder, 2015), and air pollutant monitoring (Fuentes, 2002). Simple models assume second-order stationarity of the spatial process; however, this can be unrealistic since data are collected over heterogeneous domains. Here, the spatial processes can exhibit localized spatial behaviors. Although several methods (cf. Fuentes, 2002; Risser and Calder, 2015; Heaton et al., 2017) have been developed for modeling nonstationary spatial data, these have focused primarily on Gaussian spatial data. Moreover, fitting these models poses both computational and inferential challenges, especially for large datasets. In this manuscript, we propose a scalable algorithm for fitting nonstationary non-Gaussian datasets. Our approach captures nonstationarity by partitioning the spatial domain and modeling local spatial processes using basis expansions. This new algorithm is computationally efficient in that: (1) partitioning the spatial domain permits parallelized computation on high-performance computation (HPC) systems; and (2) basis approximation of spatial processes dramatically reduces the computational overhead.

There is a growing literature on modeling nonstationary spatial datasets. Weighted average methods (Fuentes, 2001; Kim et al., 2005; Risser and Calder, 2015) combine localized spatial models to reduce computational costs. Basis function approximations (Nychka et al., 2002; Katzfuss, 2013, 2017; Hefley et al., 2017) represent complex spatial processes using linear combinations of spatial basis functions. Higdon (1998) and Paciorek and

Schervish (2006) represent a nonstationary process using convolutions of spatially varying kernel functions. Based on the spatial partitioning strategies, some of these approaches are amenable to massive spatial datasets. For example, Heaton et al. (2017) develops a computationally efficient approach for large nonstationary spatial data by partitioning an entire domain into disjoint sets using a hierarchical clustering algorithm. Katzfuss (2017) constructs basis functions at multiple levels of resolution based on recursive partitioning of the spatial region. Guhaniyogi and Banerjee (2018) proposes a divide-and-conquer approach to generate a global posterior distribution by combining local posterior distributions from each subsample. Though these approaches scale well, they are limited to Gaussian responses.

Spatial generalized linear mixed models (SGLMMs) (Diggle et al., 1998) are popular class of models designed for non-Gaussian spatial datasets. SGLMMs are widely used for both areal and point-referenced data, where latent Gaussian random fields can account for the spatial correlations. However, fitting SGLMMs for massive spatial datasets is computationally demanding since the dimension of correlated spatial processes grows with an increasing number of observations. Although several computational methods (Banerjee et al., 2008; Hughes and Haran, 2013; Guan and Haran, 2018; Lee and Haran, 2019; Zilber and Katzfuss, 2020) have been proposed for large non-Gaussian spatial datasets, these methods assume second-order stationarity of the latent spatial processes.

In this manuscript, we propose a scalable approach for modeling massive nonstationary non-Gaussian spatial datasets. Our smooth mosaic basis approximation for nonstationary SGLMMs (SMB-SGLMMs) combines key ideas from weighted average approaches and basis

approximations. SMB-SGLMM consists of four steps: (1) partition the spatial region using a spatial clustering algorithm (Heaton et al., 2017); (2) generate localized spatial basis functions; (3) fit a nonstationary basis-representation model to each partition; and (4) smooth the local processes using distance-based weighting scheme (smooth mosaic). Due to the partitioning and localized model fitting, we can leverage parallel computing, which greatly increases the scalability of the SMB-SGLMM method. To our knowledge, this study is the first attempt to develop a scalable algorithm for fitting large nonstationary non-Gaussian spatial datasets. Furthermore, our method provides an automated mechanism for selecting appropriate spatial basis functions. We also provide ready-to-use code written in `nimble` (de Valpine et al., 2017), a software environment for Bayesian inference.

The outline for the remainder of this paper is as follows. In Section 2, we introduce several nonstationary modeling approaches. We discuss the potential extension of stationary SGLMMs to nonstationary SGLMMs and discuss their challenges. In Section 3, we propose SMB-SGLMMs for massive spatial data and provide implementation details. Furthermore, we investigate the computational complexity of our method in detail. In Section 4, we study the performance of SMB-SGLMMs through simulated data examples. In Section 5, we apply SMB-SGLMMs to malaria incidence data and binary cloud mask data from satellite imagery. We conclude with a discussion and summary in Section 6.

2 Nonstationary Modeling for Non-Gaussian Spatial Data

Let $\mathbf{Z} = \{Z(\mathbf{s}_i)\}_{i=1}^N$ be the observed data and $\mathbf{X} \subset \mathbb{R}^{N \times p}$ be the matrix of covariates at the spatial locations $\mathbf{s} = \{\mathbf{s}_i\}_{i=1}^N$ in a spatial domain $\mathcal{S} \subseteq \mathbb{R}^2$. $\mathbf{W} = \{W(\mathbf{s}_i)\}_{i=1}^N$ is a mean-zero Gaussian process with covariance matrix $\Sigma \subset \mathbb{R}^{N \times N}$. Then SGLMMs can be defined as

$$g\{\mathbb{E}[\mathbf{Z}|\boldsymbol{\beta}, \mathbf{W}]\} := \boldsymbol{\eta} = \mathbf{X}\boldsymbol{\beta} + \mathbf{W}$$
$$\mathbf{W} \sim N(0, \Sigma)$$

(1)

with link function $g(\cdot)$ and linear predictor $\boldsymbol{\eta}$. Standard SGLMMs (Diggle et al., 1998) consider a second-order stationary Gaussian process for $\mathbf{W}$ for their convenient mathematical framework. However, this assumption can be unrealistic for spatial processes existing in large heterogeneous domains (see Bradley et al. (2016), for a discussion). A natural extension to (1) is to model $\mathbf{W}$ as a nonstationary spatial process. There is an extensive literature on modeling nonstationary spatial data (Sampson, 2010) such as: (1) weighted-average methods, (2) basis function methods, and (3) process convolutions. Our method is motivated by these nonstationary modeling approaches.

Weighted average methods (Fuentes, 2001) divide the spatial region $\mathcal{S}$ into disjoint partitions and fit locally stationary models to each partition. For example, Kim et al. (2005); Heaton et al. (2017) partition the spatial domain through Voronoi tessellation. Then, the global process is constructed by combining the locally stationary processes via a weighted average. The weights are computed using the distances between the observation

locations and 'center' of the localized processes. These approaches scale well by taking advantage of parallel computation (cf. Risser and Calder, 2015; Heaton et al., 2017).

Basis functions approaches represent the nonstationary covariance structure as an expansion of spatial basis functions $\{\Phi_j(\mathbf{s})\}_{j=1}^m$. Let $\boldsymbol{\Phi}$ be an N by m matrix with columns indicate the basis functions and rows indicate locations $\boldsymbol{\Phi}_{i,j} = \Phi_j(\mathbf{s}_i)$. Then we can construct a nonstationary spatial process as

$$\mathbf{W} \approx \boldsymbol{\Phi}\boldsymbol{\delta}, \quad \boldsymbol{\delta} \sim N(0, \boldsymbol{\Sigma}_{\boldsymbol{\Phi}}),$$

where $\boldsymbol{\delta}$ is the coefficients of basis functions. We approximate the covariance structure as $\boldsymbol{\Phi}\boldsymbol{\Sigma}_{\boldsymbol{\Phi}}\boldsymbol{\Phi}^\top$, which is not dependent solely on the lag between locations; hence this is nonstationary. Different types of basis functions have been used, for instance eigenfunctions obtained from the empirical covariance (Holland et al., 1999), multiresolution basis functions (Nychka et al., 2002, 2015; Katzfuss, 2017), and computationally efficient low-rank representation of nonstationary covariance (Katzfuss, 2013).

Process convolutions represent the nonstationary spatial processes through convolutions of spatially varying kernel function and Brownian motion. For an arbitrary $\mathbf{s} \in \mathcal{S}$,

$$\mathbf{W}(\mathbf{s}) = \int_{\mathcal{S}} K_{\mathbf{s}}(\mathbf{u}) d\mathbf{W}(\mathbf{u})$$

where $K_{\mathbf{s}}(\cdot)$ is a kernel function centered at location $\mathbf{s}$ and $\mathbf{W}(\cdot)$ is a bivariate Brownian motion. Higdon (1998) use bivariate Gaussian kernels under this framework. Several extensions have also been proposed including creating closed-form nonstationary Matérn

covariance functions (Paciorek and Schervish, 2006), extension to multivariate spatial process (Kleiber and Nychka, 2012), and computationally efficient local likelihood approaches (Risser and Calder, 2015).

We note that these nonstationary models have focused on Gaussian responses. Direct application of these methods to (1) is challenging because we cannot obtain closed-form maximum likelihood estimates by marginalizing out $\mathbf{W}$. Within the Bayesian framework, updating conditional posterior distributions requires a computational complexity of $\mathcal{O}(N^3)$, which becomes infeasible even for moderately large size datasets (e.g., binary satellite data with 100,000 observations). Although several computationally efficient approaches (cf. Rue et al., 2009; Hughes and Haran, 2013; Guan and Haran, 2018; Lee and Haran, 2019; Zilber and Katzfuss, 2020) have been developed for non-Gaussian hierarchical spatial models, they are assuming stationarity of $\mathbf{W}$. In what follows, we develop partitioned nonstationary models for non-Gaussian spatial data. Our method is computationally efficient and provides accurate predictions over large heterogeneous spatial domains.

3   Smooth Mosaic Basis Approximation for Nonstationary SGLMMs

We propose a smooth mosaic basis approximation for nonstationary SGLMMs (SMB-SGLMMs) designed for massive spatial datasets. We begin with an outline of our method:

Step 1. Partition the spatial domain into disjoint subregions.

Step 2. Construct data-driven basis functions for each subregion.

Step 3. Fit a locally nonstationary basis function model to each subregion in parallel.

Step 4. Construct the global nonstationary process as a weighted average of local processes.

SMB-SGLMMs are described in Figure 1. We provide the details in the following subsections.

3.1 Partitioned Nonstationary Spatial Models

Step 1. Partition the spatial domain into disjoint subregions

We use an agglomerative clustering approach (Heaton et al., 2017) to partition the spatial domain $\mathcal{S}$ into K subregions $\{\mathcal{S}_k\}_{k=1}^K$, which satisfy $\cup_{k=1}^K \mathcal{S}_k = \mathcal{S}$. We fit a nonspatial generalized linear model (`glm` function in `R`) using responses $\mathbf{Z}$ and covariates $\mathbf{X}$. Then we obtain the spatially correlated residuals $\{\epsilon(\mathbf{s}_i)\}_{i=1}^N$. For all $i \neq j$, we calculate the dissimilarity between $\epsilon(\mathbf{s}_i)$ and $\epsilon(\mathbf{s}_i)$ as $d_{ij} = |\epsilon(\mathbf{s}_i) - \epsilon(\mathbf{s}_j)|/\|\mathbf{s}_i - \mathbf{s}_j\|$ from spatial finite differences (Banerjee and Gelfand, 2006). Heaton et al. (2017) assigns locations with low dissimilarity values (d_{ij}) into the same partitions. The main idea is to separate locations with large pairwise dissimilarities (i.e. rapidly changing residual surfaces $\epsilon(\mathbf{s})$). We initialize $K = N$ where each observation belongs to its own cluster. Then we combine two clusters if they are Voronoi neighbors and have minimum pairwise dissimilarity. We repeat this procedure until we arrive at the desired K partitions (Figure 1 (a)). We provide details about the clustering algorithm in the supplementary material.
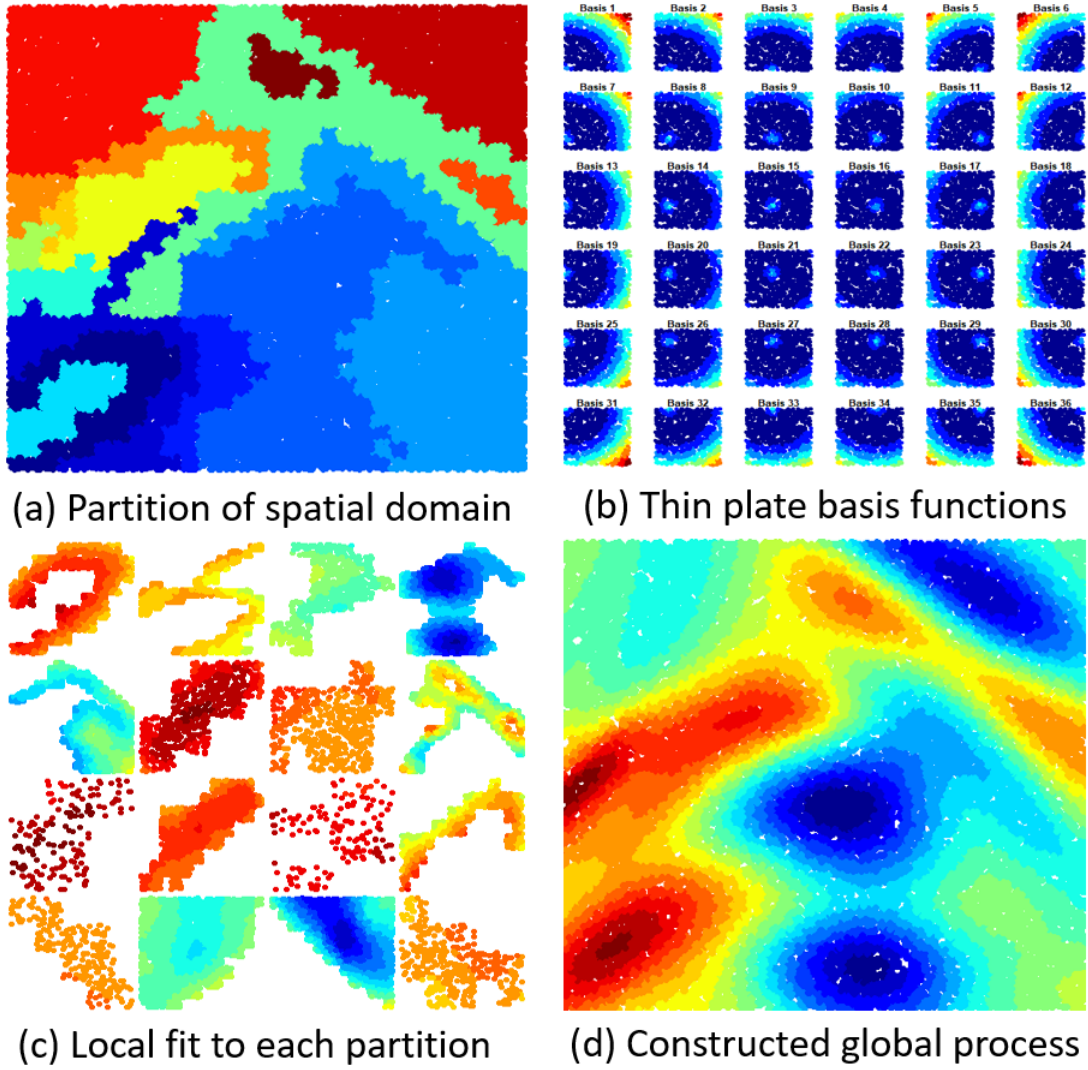
(a) Partition of spatial domain

(b) Thin plate basis functions

(c) Local fit to each partition

(d) Constructed global process

Figure 1: Illustration for the partitioned nonstationary approach for simulated $\mathbf{W}$. (a) Nonstationary $\mathbf{W}$ is partitioned through 16 subregions; different colors indicate disjoint partitions. (b) For each partition, thin plate splines basis functions are constructed at knots; basis functions represent distinct spatial patterns. (c) The Local nonstationary model is fit to each partition using a linear combination of basis functions. (d) The global nonstationary process is obtained via a weighted average of the local processes.

9

Step 2. Construct data-driven basis functions for each subregion

For each partition, we generate a collection of spatial basis functions. We have $\mathbf{Z}_k = \{Z(\mathbf{s}) : \mathbf{s} \in \mathcal{S}_k\} \in \mathbb{R}^{N_k}$, the observations belong to $\mathcal{S}_k$, where $N = \sum_{k=1}^{K} N_k$. $\mathbf{X}_k$ is an $N_k \times p$ matrix of covariates. Consider the knots (grid points) $\{\mathbf{u}_{kj}\}_{j=1}^{m_k}$ over $\mathcal{S}_k$ ($m_k \ll N_k$). These knots can define a wide array of spatial basis functions such as radial basis functions (Nychka et al., 2015; Katzfuss, 2017) and eigenbasis functions (Banerjee et al., 2008). In this study, we consider thin plate splines defined as $\Phi_{kj}(\mathbf{s}) = \|\mathbf{s} - \mathbf{u}_{kj}\|^2 \log(\|\mathbf{s} - \mathbf{u}_{kj}\|)$. Here $\mathbf{\Phi}_k$ is an $N_k \times m_k$ matrix by evaluating the basis function at N_k locations in $\mathcal{S}_k$ (Figure 1 (b)). Although we focus on thin plate splines, different types of basis functions can be considered. Examples include eigenfunctions (Holland et al., 1999; Banerjee et al., 2013; Guan and Haran, 2018), radial basis (Nychka et al., 2015; Katzfuss, 2017), principal components (Higdon et al., 2008; Cressie, 2015), and Moran's basis (Hughes and Haran, 2013; Lee and Haran, 2019).

Step 3. Fit a locally nonstationary basis function model to each subregion in parallel.

For each partition, we can represent the spatial random effects as $\mathbf{W}_k \approx \mathbf{\Phi}_k \boldsymbol{\delta}_k$ and model the conditional mean $\mathbb{E}[\mathbf{Z}_k | \boldsymbol{\beta}_k, \mathbf{\Phi}_k, \boldsymbol{\delta}_k]$ as

$$g\{\mathbb{E}[\mathbf{Z}_k | \boldsymbol{\beta}_k, \mathbf{\Phi}_k, \boldsymbol{\delta}_k]\} := \boldsymbol{\eta}_k = \mathbf{X}_k \boldsymbol{\beta}_k + \mathbf{\Phi}_k \boldsymbol{\delta}_k$$

$$\boldsymbol{\delta}_k \sim N(0, \mathbf{\Sigma}_{\mathbf{\Phi}_k}),$$

(2)

where $\boldsymbol{\Sigma_{\Phi_k}}$ is a covariance of basis coefficients $\boldsymbol{\delta}_k$. Here we set $\boldsymbol{\Sigma_{\Phi_k}} = \sigma_k^2 \mathbf{I}_k$, as in a discrete approximation of a nontationary Gaussian process (Higdon, 1998). This basis representation approximates the covariance through $\sigma_k^2 \boldsymbol{\Phi}_k \boldsymbol{\Phi}_k^\top$. Such approximation can capture the nonstationary behavior of the spatial process through a linear combination of basis functions (Figure 1 (c)). Since we typically choose $m_k \ll N_k$, basis representations can drastically reduce computational costs by avoiding large matrix operations. For our simulated example (Section 4.1), we use $m_k = 81$ for a partition of size $N_k = 13,129$. We provide implementation details in Section 3.2. In addition, a clever choice of $\boldsymbol{\Phi}_k$ can also reduce correlations in $\boldsymbol{\delta}_k$, resulting in fast mixing MCMC algorithms (Haran et al., 2003; Christensen et al., 2006). For the exponential family distribution $f(\cdot)$, the partition-specific hierarchical spatial model is as follows:

$$
\begin{aligned}
\textbf{Data Model:} \qquad & \mathbf{Z}_k | \boldsymbol{\eta}_k \sim f(\boldsymbol{\eta}_k) \\[4pt]
& g\{\mathbb{E}[\mathbf{Z}_k | \beta_k, \boldsymbol{\Phi}_k, \boldsymbol{\delta}_k)]\} := \boldsymbol{\eta}_k = \mathbf{X}_k \beta_k + \Phi_k \boldsymbol{\delta}_k \\[4pt]
\textbf{Process Model:} \qquad & \boldsymbol{\delta}_k | \sigma_k^2 \sim N(0, \sigma_k^2 \mathbf{I}_k) \\[4pt]
\textbf{Parameter Model:} \qquad & \beta_k \sim p(\beta_k), \sigma_k^2 \sim p(\sigma_k^2)
\end{aligned}
\tag{3}
$$

We complete the hierarchical model by assigning prior distributions for the model parameters β_k and σ_k^2.

Step 4. Construct the global nonstationary process as a weighted average of the local processes.

To construct the global process, we use a weighted average of the fitted local processes. Note that $\mathbf{\Phi}_k \in \mathbb{R}^{N_k \times m_k}$ is the basis functions matrix consisting of thin plate splines $\Phi_{kj}(\mathbf{s}) = \|\mathbf{s} - \mathbf{u}_{kj}\|^2 \log(\|\mathbf{s} - \mathbf{u}_{kj}\|)$ for $s \in \mathcal{S}_k$, where $\{\mathbf{u}_{kj}\}_{j=1}^{m_k}$ are the knots over $\mathcal{S}_k$. Here, we introduce another notation. We define $\widetilde{\mathbf{\Phi}}_k \in \mathbb{R}^{N \times m_k}$ by evaluating $\Phi_{kj}(\mathbf{s})$ for all $s \in \mathcal{S}$. Let $\widetilde{\mathbf{\Phi}}_k(\mathbf{s}) \in \mathbb{R}^{m_k}$ be the row of $\widetilde{\mathbf{\Phi}}_k$ corresponding to spatial location $\mathbf{s} \in \mathcal{S}$. Since $\mathbf{W_k}(\mathbf{s}) \approx \widetilde{\mathbf{\Phi}}_k^\top(\mathbf{s})\boldsymbol{\delta}_k$, we have:

$$\mathbf{W}(\mathbf{s}) = \sum_{k=1}^{K} c_k(\mathbf{s})\mathbf{W_k}(\mathbf{s}) \approx \sum_{k=1}^{K} c_k(\mathbf{s})\widetilde{\mathbf{\Phi}}_k^\top(\mathbf{s})\boldsymbol{\delta}_k,$$

$$c_k(\mathbf{s}) \propto \exp\left(-\|\mathbf{s} - \widetilde{\mathbf{s}}_k\|^2\right) \text{ if } \|\mathbf{s} - \widetilde{\mathbf{s}}_k\| \le \gamma \text{ otherwise } 0,$$

(4)

where $\widetilde{\mathbf{s}}_k \in \mathcal{S}_k$ is the closest point to $\mathbf{s}$. The weight $c_k(\mathbf{s})$ is proportional to the inverse distance between $\mathbf{s}$ and $\widetilde{\mathbf{s}}_k$; hence, shorter distances result in higher weights. We assign a 0 weight if the distance exceeds a threshold, or weighting radius, γ. We present details about choice of γ in Section 3.2. The weighted average of the local processes approximates the nonstationary global process (Figure 1 (d)). Similarly, a global linear predictor $\boldsymbol{\eta}$ can be written as

$$\boldsymbol{\eta}(\mathbf{s}) = \sum_{k=1}^{K}[\mathbf{X}(\mathbf{s})^\top\boldsymbol{\beta}_k\mathbf{1}_{\{\mathbf{s}\in\mathcal{S}_k\}} + c_k(\mathbf{s})\widetilde{\mathbf{\Phi}}_k^\top(\mathbf{s})\boldsymbol{\delta}_k],$$

(5)

where $\mathbf{1}_{\{\mathbf{s}\in\mathcal{S}_k\}}$ is an indicator function. Here $\mathbf{X}(s) \in \mathbb{R}^p$ is a vector of the covariate matrix $\mathbf{X}$ for location $\mathbf{s}$, $\boldsymbol{\beta}_k \in \mathbb{R}^p$ is corresponding regression coefficients. Our method provides a partition varying estimate of $\boldsymbol{\beta}_k$. This is because the fixed effects may have spatially

12

varying (nonstationary) behavior over large heterogeneous spatial domains. Therefore, as in Heaton et al. (2017) we provide a partition varying $\boldsymbol{\beta}_k$ in our applications. If estimating a global $\boldsymbol{\beta}$ is of interest, one may consider divide and conquer algorithms such as consensus Monte Carlo (Scott et al., 2016) or geometric median of the subset posteriors (Minsker et al., 2017). Such methods provide the global posterior distribution of fixed effects by combining subset posteriors.

Spatial prediction

Spatial prediction at unobserved locations is of great interest in many scientific applications. Let $\mathbf{s}^* \in \mathcal{S}$ be an arbitrary unobserved location. From thin plate splines basis functions, we can construct a local basis as $\Phi_{kj}(\mathbf{s}^*) = \|\mathbf{s}^* - \mathbf{u}_{kj}\|^2 \log(\|\mathbf{s}^* - \mathbf{u}_{kj}\|)$, where we have $\{u_{kj}\}_{j=1}^{m_k}$ knots in partition k. As in (5) we can also provide a global prediction:

$$\boldsymbol{\eta}(\mathbf{s}^*) = \sum_{k=1}^{K} [\mathbf{X}(\mathbf{s}^*)^\top \boldsymbol{\beta}_k \mathbf{1}_{\{\mathbf{s}^* \in \mathcal{S}_k\}} + c_k(\mathbf{s}^*) \widetilde{\boldsymbol{\Phi}}_k^\top(\mathbf{s}^*) \boldsymbol{\delta}_k]. \tag{6}$$

For given posterior samples $\{\boldsymbol{\beta}_k, \boldsymbol{\delta}_k\}_{k=1}^{K}$, we can obtain a posterior predictive distribution of $\boldsymbol{\eta}(\mathbf{s}^*)$.

3.2   Implementation Details

In this section, we provide automated heuristics for the tuning parameters. To implement SMB-SGLMMs, we need to specify the following components: (1) K number of partitions, (2) location of knots in each partition, and (3) a weighting radius γ for smoothing the local processes. In practice, we can set $K \leq C$ (number of available cores) for parallel

computation. Our method is heavily parallelizable, so computational walltimes tend to decrease with larger K. However, selecting a very large K may result in unreliable local estimates due to a small number of observations N_k within each partition. In our simulation study, we compare the performance of our approach with varying K. Then, we select the K that minimizes the out-of-sample root cross validated mean squared prediction error (rCVMSPE). Based on simulation results, the SMB-SGLMM is robust to the choice of K.

To avoid overfitting, we use lasso (Tibshirani, 1996) to select the appropriate number and location of the knots. Initially, we set m candidate knots $\{\mathbf{u}_{kj}\}_{j=1}^{m}$ uniformly over each partition $\mathcal{S}_k$ (e.g. $m \approx 1000$). Then we fit a penalized glm with lasso using response $\mathbf{Z}_k$ and covariates $[\mathbf{X}_k, \mathbf{\Phi}_k]$, where $\mathbf{\Phi}_k$ is an N_k by m matrix. We impose an l_1 penalty to only the basis coefficients $\boldsymbol{\delta}_k$, not the fixed effects $\boldsymbol{\beta}_k$. We use the `glmnet` package (Friedman et al., 2010a) in `R` for lasso regression. For basis selection, we choose the basis functions corresponding to the nonzero basis coefficients. Since we run lasso regression independently for each partition, this step is embarrassingly parallel.

From a pre-specified set of values (e.g., $\gamma = 0.01, 0.025, 0.05, 0.1$), we choose the γ that yields the lowest rCVMSPE. Note that we choose γ upon completion of Steps 1-3, the computationally demanding parts of SMB-SGLMM. Since the calculations in (6) are inexpensive, there are very little additional costs associated with Step 4.

3.3   Computational Complexity

We examine the computational complexity of SMB-SGLMM and illustrate how our approach scales with an increasing number of observations N. The three computationally

demanding components are (1) basis selection (lasso), (2) MCMC for fitting the local pro-
cesses, and (3) obtaining the global process. Here, parallelized computing is integral to the
scalability of SMB-SGLMM. We provide the following discussion on computational costs
and parallelization for each step:

1. **Basis Selection:** In each partition, our methods select the m_k knots from m can-
   didates using a regularization method (lasso). Based on results in Friedman et al.
   (2010a) the cost of the coordinate descent-based lasso is $\mathcal{O}(N_k m)$, where N_k is the
   number of observations in a partition $\mathcal{S}_k$. We can select the basis functions for each
   partition in parallel across K processors.

2. **MCMC for local processes:** The computational cost is dominated by matrix-
   vector multiplications $\boldsymbol{\Phi}_k \boldsymbol{\delta}_k$, where $\boldsymbol{\Phi}_k$ is the N_k by m_k basis function matrix from
   the previous lasso step. The costs for this step is $\mathcal{O}(N_k m_k)$. We can fit the local
   processes in parallel across K processors.

3. **Global Process:** We obtain the global process using weighted averages in (4). This
   step requires $\mathcal{O}(N^2)$ complexity to calculate a distance matrix because the weights
   $c_k(\mathbf{s})$ in (4) are based on the distances between observations. Computing $c_k(\mathbf{s})$ requires
   a one-time computation of the distance matrix for all N locations, which can be
   readily parallelized across C available processors. We propose a novel way to "stream"
   the distances (Supplement) so that we can compute the weights $c_k(\mathbf{s})$ without actually
   storing the final distance matrix (e.g. 8TB for $N = 1$ million).

Table 1 summarizes complexity of SMB-SGLMM. Considering that the complexity of

Operations	Complexity
Basis selection	$\mathcal{O}(\sum_{k=1}^{K} N_k m/K)$
MCMC	$\mathcal{O}(\sum_{k=1}^{K} N_k m_k/K)$
Weighted average	$\mathcal{O}(N^2/C)$

Table 1: Computational complexity of SMB-SGLMMs. K is the number of partitions and C is the total available cores. N_k is the number of observations, and m_k is the number of knots from each partition. Knots are selected from m candidate knots using a lasso.

the stationary SGLMM is $\mathcal{O}(N^3)$, SMB-SGLMM is fast and provides accurate predictions for nonstationary processes (details in Sections 4,5).

4   Simulated Data Examples

We implement SMB-SGLMMs in two simulated examples of massive ($N = 100,000$) non-stationary binary and count data. We implement our approach in `nimble` (de Valpine et al., 2017), a programming language for constructing and fitting Bayesian hierarchical models. Parallel computation is implemented through the `parallel` package in `R`. The computation times are based on a single 2.2 GHz Intel Xeon E5-2650v4 processor. All the code was run on the Pennsylvania State University Institute for Cyber Science-Advanced Cyber Infrastructure (ICS-ACI) high-performance computing infrastructure. Source code is provided in the Supplement.

Data is generated on $125,000$ locations on the spatial domain $\mathcal{S} \in \mathbb{R}^2$. We fit the spatial models using $N = 100,000$ observations and reserve the remaining $N_{cv} = 25,000$ observations for validation. We denote the model-fitting observations as $\mathbf{Z} = \{Z(s_i) : s_i \in \mathbf{s}\}$ where $\mathbf{s} = \{s_1, ..., s_N\}$. Observations are generated using the SGLMM framework described in (1) with $\boldsymbol{\beta} = (1, 1)$. The nonstationary spatial random effects $\mathbf{W} = \{W(s_i) :$

16

$s_i \in \mathbf{s}\}$ are generated through convolving spatially varying kernel functions (Higdon, 1998; Paciorek and Schervish, 2006; Risser and Calder, 2015). For some $s \in \mathbf{s}$ and reference locations $u_j \in \mathcal{D}$, we have $\mathbf{W}(s) = \sum_{j=1}^{J} K_s(u_j)V(u_j)$, where $K_s(u_j)$ is a spatially varying Gaussian kernel function centered at reference location u_j and $V(u_j)$ is a realization of Gaussian white noise. Additional details are provided in the Supplement. The binary dataset uses a Bernoulli data model and a logit link function $\text{logit}(p) = \frac{p}{1-p}$, and the count dataset is similarly generated using a Poisson data model and a log link function.

We model the localized processes using the hierarchical framework in (3). To complete the hierarchical model, we set priors following Hughes and Haran (2013): $\beta \sim N(\mathbf{0}, 100I)$ and $\sigma^2 \sim IG(0.5, 2000)$. We study SMB-SGLMM for different combinations of K (the number of partitions) and γ (weighting radius). We examine five partition groups $K = \{4, 9, 16, 25, 36\}$ and four weighting radii $\gamma = \{0.1, 0.25, 0.5, 1\}$. In total, we study a total of $5 \times 4 = 20$ implementation.

For each case, we perform basis selection via lasso using the `glmnet` R package (Friedman et al., 2010b). We generate $100,000$ samples from the posterior distribution $\pi(\boldsymbol{\beta}, \boldsymbol{\delta}, \sigma^2)$ using a block random-walk Metropolis-Hastings algorithm using the adaptation routine from Shaby and Wells (2010). We examine predictive ability and computational cost. These include $\text{rCVMSPE} = \sqrt{\frac{1}{N_{cv}} \sum_{i=1}^{N_{cv}} (Z_i - \hat{Z}_i)^2}$ and the walltime required to run $100,000$ iterations of the MCMC algorithm. In addition, we present the posterior predictive intensity and probability surfaces.

4.1 Count Data

Table 2 presents results for the out-of-sample prediction errors for the SMB-SGLMM approach. Results indicate that the performance of our approach is robust across different combinations of K and γ. For this example, predictive accuracy improves as we increase the number of partitions (K) and decrease the width of the weight radius $(\gamma = 0.1)$. We provide the posterior predictive intensity surface in Figure 2 for the implementation yielding the lowest rCVMSPE ($K = 36$ and $\gamma = 0.1$). Based on visual inspection, the SMB-SGLMM approach captures the nonstationary behavior of the true latent spatial process.

We report the combined walltimes for running lasso, MCMC, and weighting. Walltimes decrease considerably as we increase the number of partitions. This is not surprising as we fit these models in parallel and the sample size for each partition tends to decrease as we increase the number of total partitions. For each partition, model fitting incurs a computational cost of $\mathcal{O}(N_k m_k)$ where N_k and m_k are the number of observations and the number of selected basis functions (thin-plate splines) within partition k, respectively. For the case where $K = 36$, the median number of basis functions per partition is 14 with a range of 4 to 169.

The localized parameter estimates of $\boldsymbol{\beta}$ are centered around the true parameter values $\boldsymbol{\beta} = (1, 1)$ (Supplement). For the case where the number of partitions $K = 36$, we also provide a map of the localized estimates of $\boldsymbol{\beta} = (\beta_1, \beta_2)$ in the Supplement.
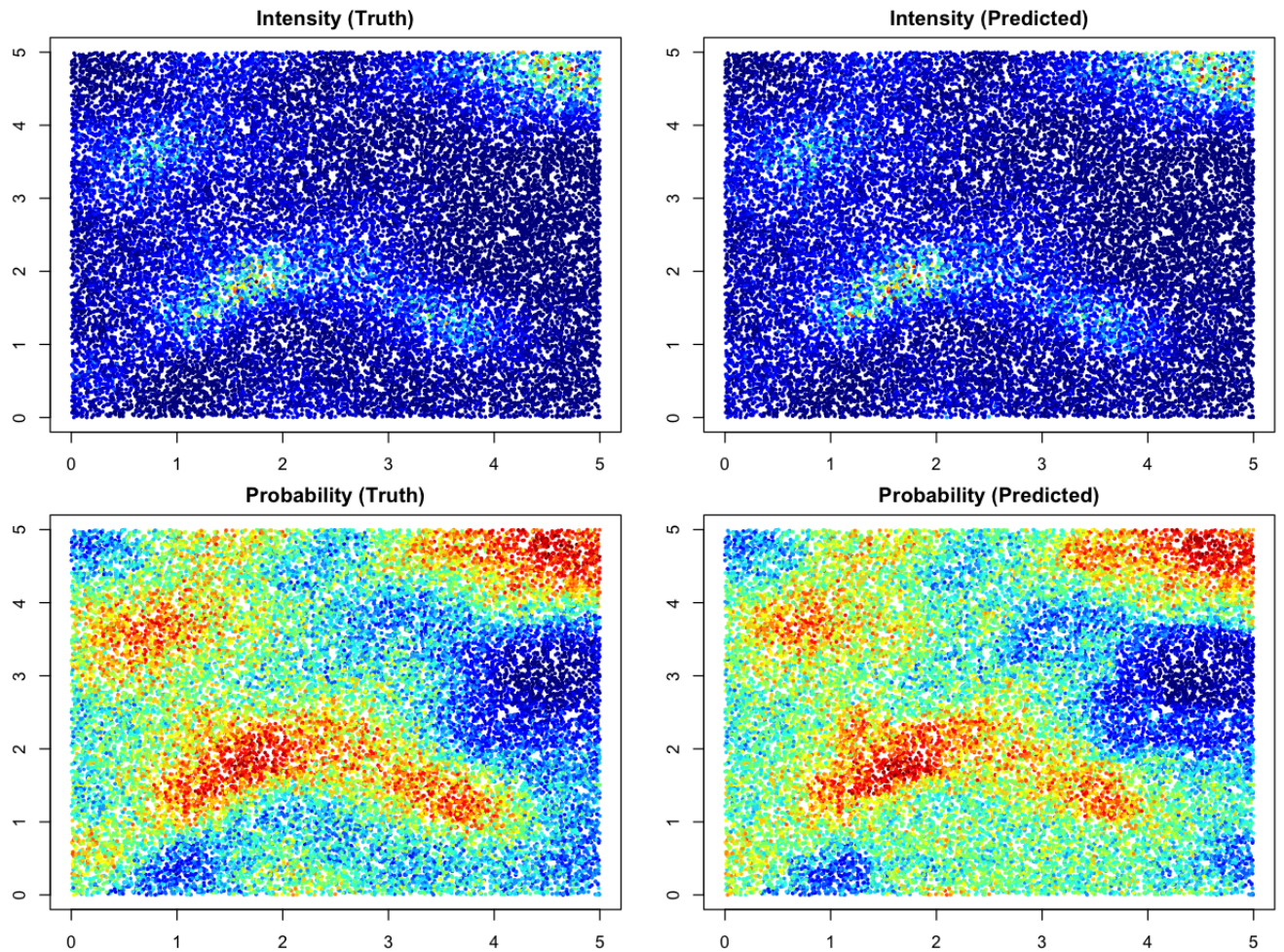
Figure 2: True (top left) and predicted intensity surfaces (top right) for the simulated count data example. True (bottom left) and predicted probability surfaces (top right) for the simulated binary data example. We set $K = 36$ and $\gamma = 0.1$ for the count example and $K = 25$ and $\gamma = 0.1$ for the binary case.

| | Weighting Radius (γ) | | | | Walltime |
Partitions	0.1	0.25	0.5	1	(minutes)
4	1.079	1.109	1.147	1.204	113.13
9	1.060	1.084	1.137	1.228	67.92
16	1.059	1.073	1.104	1.196	65.19
25	1.057	1.073	1.127	1.576	65.34
36	**1.054**	1.069	1.162	2.145	25.32

Table 2: Cross-validation root mean squared prediction error (rCVMSPE) and total wall-time (minutes) for the count data simulated example. Rows denote the five partition classes and columns correspond to the chosen weighting radius (γ). We report the combined wall-time for lasso, MCMC, and weighting.

4.2 Binary Data

In Table 3, we present prediction results for the binary simulated dataset. For this example, we observe that increasing the number of partitions K and reducing the neighbor radius γ results in more accurate predictions and lower computational costs. Figure 2 includes the posterior predictive probability surface for the implementation yielding the lowest root CVMSPE ($K = 25$ and $r = 0.1$). For the case where $K = 25$, the mean number of basis functions per partition is 7.5 with a range of 0 to 33. In addition, computational walltimes decrease considerably as we increase the number of partitions for the reasons presented in Section 4.1. The localized parameter estimates of $\boldsymbol{\beta}$ are centered around the true parameter values $\boldsymbol{\beta} = (1, 1)$ (Supplement). For the case where the number of partitions $K = 25$, we provide a map of the localized estimates of $\boldsymbol{\beta} = (\beta_1, \beta_2)$.

5 Applications

In this section, we apply our method to two real-world datasets pertaining to malaria incidence in the African Great Lakes region and cloud cover from satellite imagery. For both

Partitions	Weighting Radius (γ)				Walltime
	0.1	0.25	0.5	1	(minutes)
4	0.360	0.362	0.371	0.380	70.15
9	**0.348**	0.351	0.365	0.381	17.76
16	**0.348**	0.351	0.370	0.402	15.98
25	**0.348**	0.350	0.365	0.397	8.65
36	0.349	0.350	0.364	0.402	16.330

Table 3: Cross-validation root mean squared prediction error (rCVMSPE) and total wall-time (minutes) for the binary simulated example. Rows denote the five partition classes and columns correspond to the chosen weighting radius (γ). We report the combined walltime for lasso, MCMC, and weighting.

large non-Gaussian nonstationary datasets, SMB-SGLMM provides accurate predictions within a reasonable timeframe.

5.1 Malaria Incidence in the African Great Lakes Region

Malaria is a parasitic disease which can lead to severe illnesses and even death. Predicting occurrences at unknown locations can be of significant interest for effective control interventions. We compiled malaria incidence data from the Demographic and Health Surveys of 2015 (ICF, 2020). The dataset contains malaria incidence (counts) from $4,741$ GPS clusters in nine contiguous countries in the African Great Lakes region: Burundi, the Democratic Republic of Congo, Malawi, Mozambique, Rwanda, Tanzania, Uganda, Zambia, and Zimbabwe. We use the population size, average annual rainfall, vegetation index of the region, and the proximity to water as spatial covariates. Under a spatial regression framework, Gopal et al. (2019) analyzes malaria incidence in Kenya using these environmental variables. In this study, we extend this approach to multiple countries in the African Great Lakes region.

We use $N = 3,973$ observations to fit the model and save $N_{cv} = 948$ observations for

21

| Partitions | Weighting Radius (γ) | | | | | Walltime |
	0.035	0.075	0.1	0.2	0.3	(minutes)
2	55.1	62.7	69.4	78.6	88.2	33.2
3	58.6	69.7	76.8	95.2	132.1	19.9
4	56.9	70.7	82.1	82.2	94.2	16.9

Table 4: Root CVMSPE and total walltime (mins) for the malaria incidence example. Rows denote the four partition classes and columns correspond to the chosen weighting radius. We report the combined walltime for lasso, MCMC, and weighting.
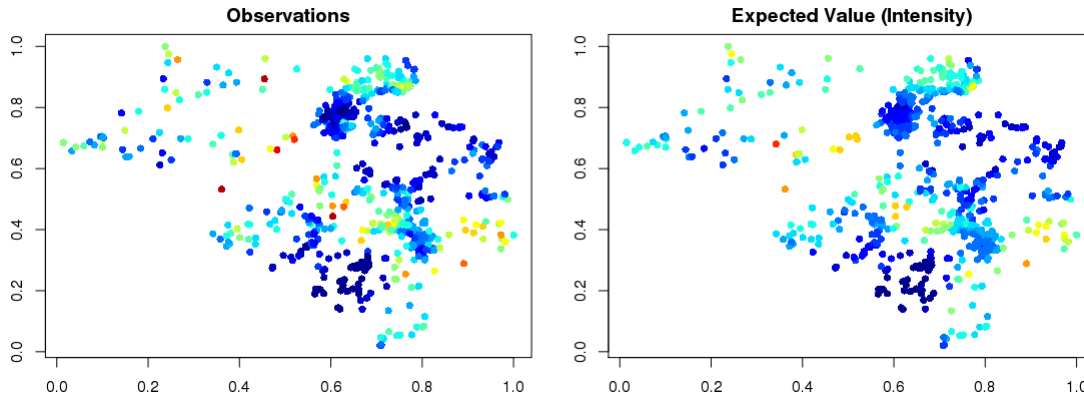

Figure 3: Illustration of the malaria occurrence dataset for $K = 2$ and $\gamma = 0.035$. True observations (left) and posterior predictive intensity surface (right) for the validation sample.

cross-validation. We study the performance of SMB-SGLMMs for different combinations of $K \in \{2, 3, 4\}$ and $\gamma \in \{0.035, 0.075, 0.1, 0.2, 0.3\}$. For each partition, we set the number of candidate knots to be approximately $m = 500$ and perform basis selection using lasso (Tibshirani, 1996). On average 49.5 basis functions are selected per partition. We fit a local spatial model (3) running the MCMC algorithm for $200,000$ iterations.

Table 4 compares the rCVMSPE for each case. We observe that rCVMSPE increases with larger weighting radii γ, possibly due to over smoothing in the partition boundaries. For smaller γ (0.035 and 0.075), we find that predictions are not sensitive to the choice of K. For this example, setting $K = 2, \gamma = 0.035$ yields the most accurate predictions. In Figure 3, the predicted intensities of the validation locations exhibit similar spatial pat-
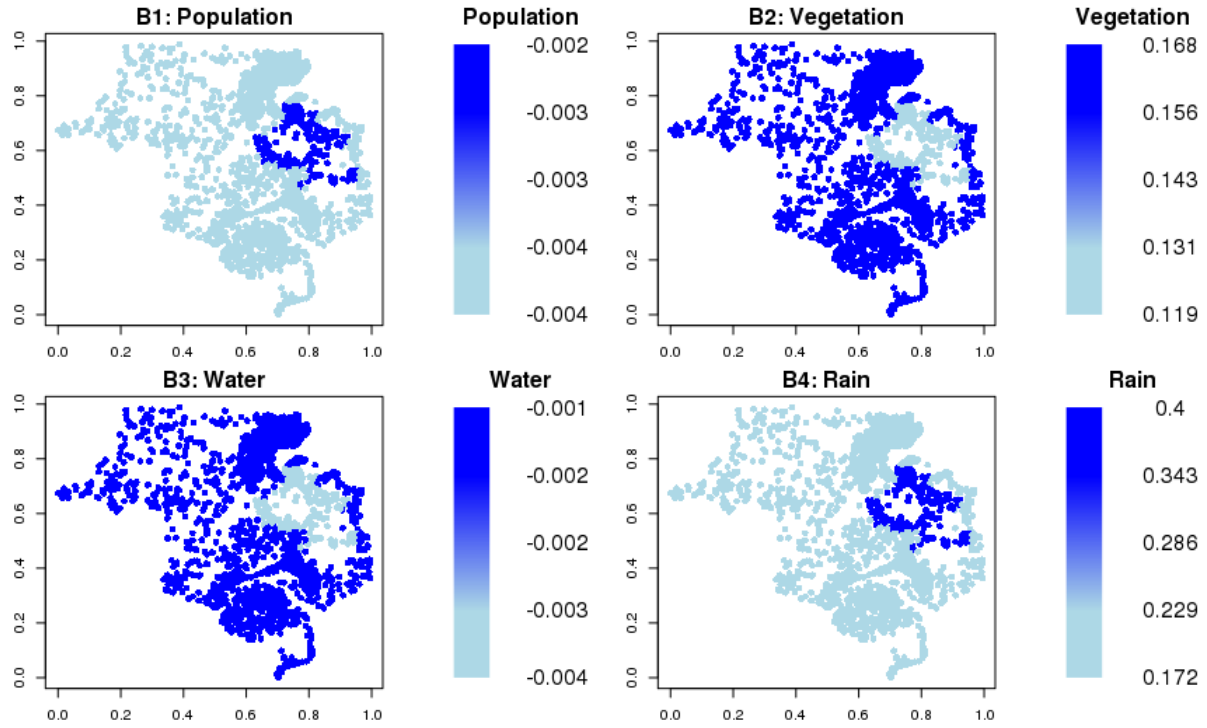
Figure 4: Posterior mean estimates of partition-varying ($K = 2$) fixed effects $\hat{\boldsymbol{\beta}}$. Estimated coefficients ($\{\hat{\beta}_1, \hat{\beta}_2, \hat{\beta}_3, \hat{\beta}_4\}$) for covariates population (top left), vegetation (top right), water (bottom left), and rain (bottom right).

terns as the true count observations. We provide maps for the partition-varying coefficients $(K = 2)$ in Figure 4. The smaller partition includes parts of northern Malawi, southern Tanzania, and northeastern Zambia. Here, the values of $\widehat{\beta} > 0$ indicate that the corresponding covariates have a positive relationship with malaria incidence. From the estimates of $\widehat{\beta}_4$, we observe that while rainfall may increase malaria incidence, these effects are more pronounced in the smaller partition.

5.2 Moderate Resolution Imaging Spectroradiometer (MODIS) Cloud Mask Data

The National Aeronautics and Space Administration (NASA) launched the Terra Satellite in December 1999 as part of the Earth Observing System. As in past studies (Sengupta and Cressie, 2013; Bradley et al., 2019), we model the cloud mask data captured by the Moderate Resolution Imaging Spectroradiometer (MODIS) instrument onboard the Terra satellite. The response is a binary incidence of cloud mask at a 1km $\times$ 1km spatial resolution. In this study, we selected $N = 1,000,000$ observations to fit our model and reserved $N_{cv} = 111,000$ for validation. We model the binary observations as a nonstationary SGLMM via the SMB-SGLMM method. Similar to Sengupta and Cressie (2013); Bradley et al. (2019), we include the vector $\mathbf{1}$ and a vector of latitudes as the covariates and use a logit link function.

For the SMB-SGLMM approach, we vary the number of partitions $K \in \{16, 25, 36, 49\}$ and weighting radius $\gamma \in \{0.01, 0.025, 0.05, 0.1\}$ for a total of 16 cases. For each partition, we begin with $m = 1,000$ knots (candidates) and perform basis selection using lasso regres-

	Weighting Radius (γ)				Walltime
Partitions	0.01	0.025	0.05	0.1	(hours)
16	0.192	0.215	0.229	0.266	5.4
25	**0.174**	0.175	0.184	0.211	3.9
36	0.182	0.200	0.223	0.299	3.2
49	0.186	0.198	0.222	0.290	2.8

Table 5: Misclassification Rate and total walltime (hours) for the MODIS cloud mask example. Rows denote the four partition classes and columns correspond to the chosen weighting radius. We report the combined walltime for lasso, MCMC, and weighting.

sion Tibshirani (1996). On average, basis selection results in roughly 16.3 basis functions per partition. For each partition, we fit a localized spatial basis SGLMM (3) by running the MCMC algorithm for $100,000$ iterations.

Figure 5 indicates that there are similar spatial patterns between binary observations and predicted probability surface. We also provide the misclassification rate for each case in Table 5. The performance of SMB-SGLMMs is robust across different choices of K and γ. Results suggest that a moderate number of partitions ($K = 25$) and a smaller weighting radius ($\gamma = 0.01$) yields the most accurate predictions. The combined walltimes decrease when using more partitions; however, these are on the order of hours in all cases.

6   Discussion

In this manuscript, we propose a scalable algorithm for modeling massive nonstationary non-Gaussian datasets. Existing approaches are limited to either stationary non-Gaussian or nonstationary Gaussian spatial data, but not both. Our method divides the spatial domain into disjoint partitions using a spatial clustering algorithm (Heaton et al., 2017). For each partition, we fit a localized model using a collection of thin plate spline basis
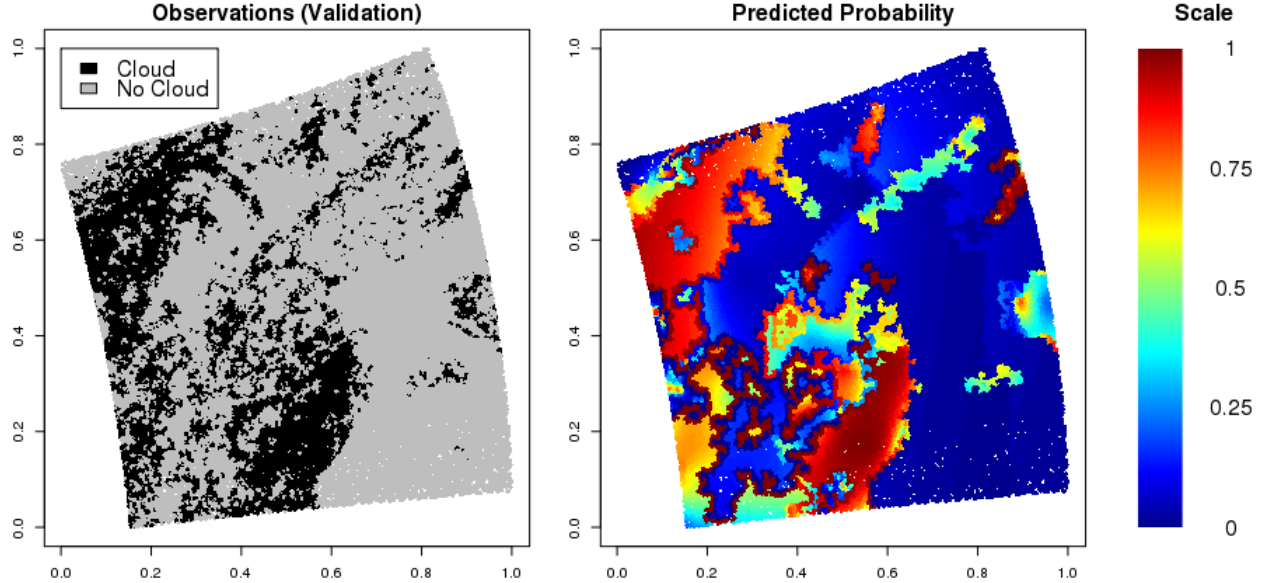
Figure 5: Illustration for the MODIS cloud mask dataset. (left) True observations of cloud mask. (right) Posterior predictive probability surface ($K = 25$ and $\gamma = 0.01$).

functions. Here, the linear combinations of the basis functions capture the underlying non-stationary behavior. We provide an automated basis selection process via a regularization approach, such as lasso. This framework is computationally efficient due to parallel computing and using basis representations of complex spatial processes. Our study shows that the proposed method provides accurate estimations and predictions within a reasonable time. Moreover, our approach scales well to massive datasets, where we model $N = 1$ million binary observations within 4 hours. To our knowledge, this is the first method geared towards modeling nonstationary non-Gaussian spatial data at this scale.

The proposed framework can be extended to a wider range of spatial basis functions. In the literature, there exists a wide array of spatial basis functions such as bi-square (radial) basis functions using varying resolutions (Cressie and Johannesson, 2008; Nychka et al., 2015; Katzfuss, 2017), empirical orthogonal functions (Cressie, 2015), predictive processes

26

(Banerjee et al., 2008), Moran's basis functions (Griffith, 2003; Hughes and Haran, 2013), wavelets (Nychka et al., 2002; Shi and Cressie, 2007), Fourier basis functions (Royle and Wikle, 2005) and Gaussian kernels (Higdon, 1998). A closer examination of adopting Bayesian regularization methods (see O'Hara et al. (2009) for a detailed review) for selecting basis functions is also an interesting future research avenue.

Developing scalable methods for modeling nonstationary non-Gaussian spatio-temporal data is challenging. The partition-based basis function representation can be integrated into existing hierarchical spatio-temporal models. For example, we can approximate the nonstationary processes using a tensor product of spatial and temporal basis functions or by constructing data-driven space-time basis functions.

Acknowledgements

Supplementary Material for A Scalable Partitioned Approach to Model Massive Nonstationary Non-Gaussian Spatial Datasets

A Spatial Clustering Algorithm

Here, we provide the clustering algorithm (Heaton et al., 2017) in detail. We obtain residuals $\boldsymbol{\epsilon}$ from a GLM fit with a response vector $\mathbf{Z} \in \mathbb{R}^N$ and a covariate matrix $\mathbf{X} \in \mathbb{R}^{N \times p}$. Let $\boldsymbol{\epsilon}_k \in \mathbb{R}^{N_k}$ be the residuals belongs to the cluster (partition) $\mathcal{S}_k$. Then we can define the dissimilarity between two clusters as

$$d(\mathcal{S}_{k_1}, \mathcal{S}_{k_2}) = \left[\frac{N_{k_1} N_{k_2}}{N_{k_1} + N_{k_2}} (\bar{\epsilon}_{k_1} - \bar{\epsilon}_{k_2})^2 \right] \frac{1}{\bar{E}},$$

where $\bar{\epsilon}_k$ is the average of $\boldsymbol{\epsilon}_k$ and $\bar{E}$ is the average Euclidean distance between points in $\mathcal{S}_{k_1}, \mathcal{S}_{k_2}$. Then the spatial clustering algorithm can be summarized as follows.

Algorithm 1 Spatial clustering algorithm (Heaton et al., 2017)

Initialize each location $\mathbf{s}_k = \mathcal{S}_k$ for $k = 1, \cdots, N$; we have N number of clusters.
1. Find clusters $\mathcal{S}_{k_1}, \mathcal{S}_{k_1}$ having the minimum $d(\mathcal{S}_{k_1}, \mathcal{S}_{k_2})$ where $\mathbf{s}_i \sim \mathbf{s}_j$ (Voronori neighbors) for $\mathbf{s}_i \in \mathcal{S}_{k_1}$ and $\mathbf{s}_j \in \mathcal{S}_{k_2}$
2. Combine two clusters
$$\mathcal{S}_{\min\{k_1, k_2\}} = \mathcal{S}_{k_1} \cup \mathcal{S}_{k_2}$$
and set
$$\mathcal{S}_{\max\{k_1, k_2\}} = \emptyset$$
Repeat 1-2 until we have $K < N$ number of clusters.

We note that Algorithm 1 becomes computationally expensive with increasing number of observations. Following suggestions in Heaton et al. (2017), we perform clustering after combining observations to a lattice $\{\mathbf{s}_l^*\}_{l=1}^L$ ($L << N$). Here, $\mathcal{N}_l = \{\mathbf{s}_i : \|\mathbf{s}_i - \mathbf{s}_l^*\| <$

$\|\mathbf{s}_i - \mathbf{s}_m^*\|\}$ is the collection of observations whose closest lattice point is $\mathbf{s}_l^*$, and $\bar{\epsilon}(\mathbf{s}_l^*) = |\mathcal{N}_l|^{-1} \sum_{s_i \in \mathcal{N}_l} \epsilon(\mathbf{s}_i)$. Then we apply Algoritm 1 to $\{\bar{\epsilon}(\mathbf{s}_l^*)\}_{l=1}^L$ rather than to $\{\epsilon(\mathbf{s}_i)\}_{i=1}^N$. Since the number of lattice points L is much smaller than the number of observations N, spatial clustering algorithm becomes computationally feasible. For instance, in our simulation studies we chose $L = 900$ for $N = 100,000$.

B   Simulation of Nonstationary Spatial Random Effects

We describe how to generate the nonstationary spatial random effects from Section 4, $\mathbf{W} = \{W(s_1), ..., W(s_n))\}$. The nonstationary spatial random effects $\mathbf{W}$ are generated by convolving a collection of spatially varying kernel functions (Higdon, 1998; Paciorek and Schervish, 2006; Risser and Calder, 2015). The construction procedure is broken down into four steps: (1) select locations for the "basis" and "reference" kernel functions; (2) construct "basis" kernels; (3) use "basis" kernels to construct "reference" kernels on a finite grid; and (4) generate non-stationary spatial random effects using the "reference kernels".

In Step 1, we select M "basis" locations $\mathbf{b} = \{b_1, ..., b_M\}$ on a coarse grid of evenly-spaced locations over the spatial domain $\mathcal{D} \in \mathbb{R}^2$. Similarly, we select J "reference" locations $\mathbf{u} = \{u_1, ..., u_J\}$ on a finer grid of evenly-space locations in $\mathcal{D}$. As in past studies (Higdon, 1998; Paciorek and Schervish, 2006; Risser and Calder, 2015), we typically select $M < J$. Figure 6 illustrates the placement of the 'basis" and "reference" locations.

In Step 2, we construct Gaussian "basis" kernels centered at each basis location $\mathbf{b}$ for
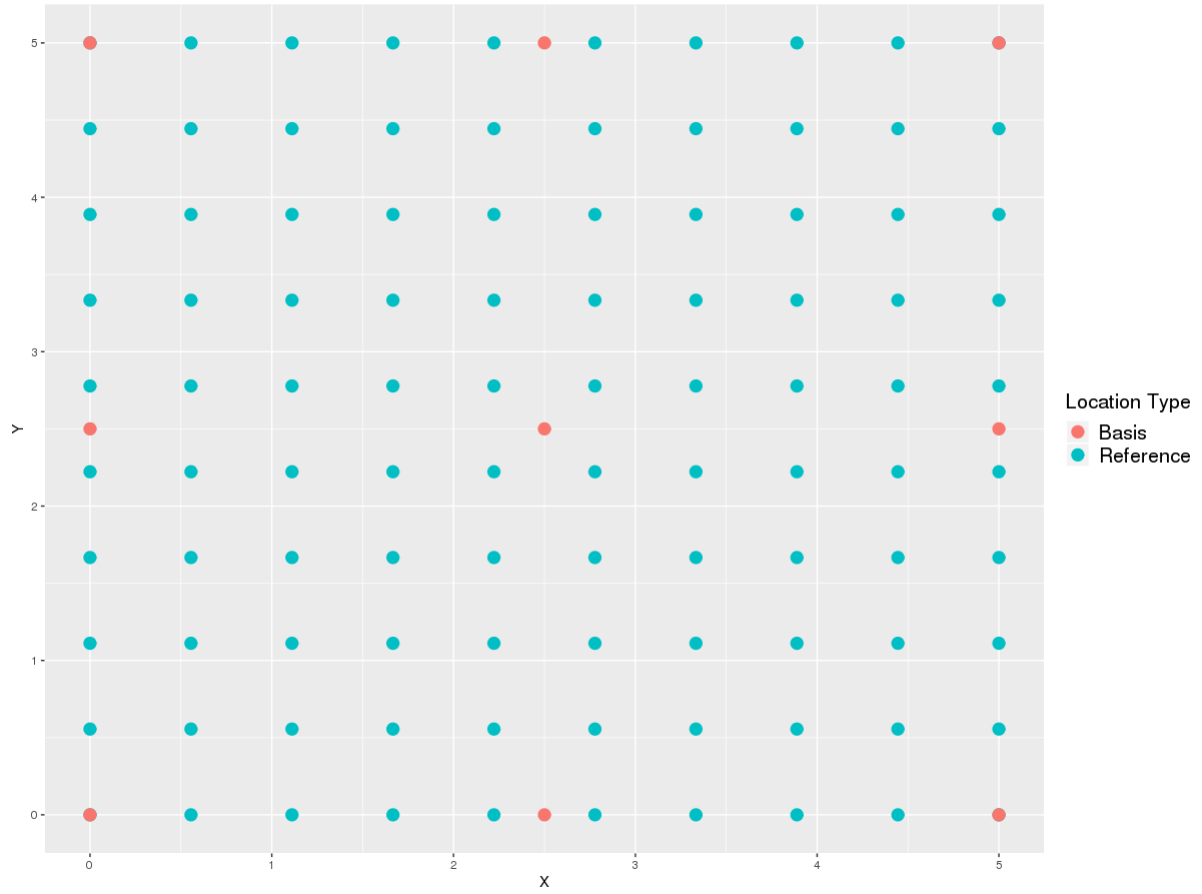
Figure 6: Locations (knots) for "basis" (red) and "reference" (blue) locations.

$m = 1, ..., M$. The "basis" kernels are defined as

$$K_m(x_i) = (2\pi)^{-1}|\Sigma_m|^{-1/2}\exp\left\{-\frac{1}{2}(x_i - b_m)'\Sigma_m(x_i - b_m)\right\},$$

where b_m is a "basis" location, x_i is the location of interest, and Σ_m is a 2×2 covariance matrix for the m-th Gaussian "basis" kernel.

In Step 3, we construct the Gaussian kernels for the reference locations $K_s(u_j)$ for $j = 1, ..., J$ as a weighted average of the "basis" kernels $K_m(\cdot)$. The "reference" kernels are defined as:

$$K_s(u_j) = \sum_{m=1}^{M} w_m(s)K_m(u_j),$$

where $w_m(s)$ are the distance-based weights, u_j are the "reference" locations, and s is the spatial location of interest. Here, the weights $w_m(s) \propto \exp\left\{-\frac{1}{2}||s - b_m||\right\}$ and $\sum_{m=1}^{M} w_m(s) = 1$.

Finally, in Step 4, we generate the nonstationary spatial random effects as

$$W(s) = \sum_{j=1}^{J} K_s(u_j)V(u_j),$$

where $K_s(u_j)$ is a spatially varying Gaussian kernel function centered at "reference" locations u_j and $V(u_j)$ is a realization of Gaussian white noise. Note that $V(u_j) \sim \mathcal{N}(0, \sigma_u^2)$.

In our implementation, we chose $M = 9$ "basis" locations $\mathbf{b} = \{b_1, ..., b_M\}$ and $J = 100$ "reference" locations $\mathbf{u} = \{u_1, ..., u_J\}$ on a grid of evenly-space locations in $\mathcal{D}$. The "basis" kernel functions $K_m(\cdot)$ for $m = 1, ..., 9$ have spatially-varying covariance matrices Σ_m as
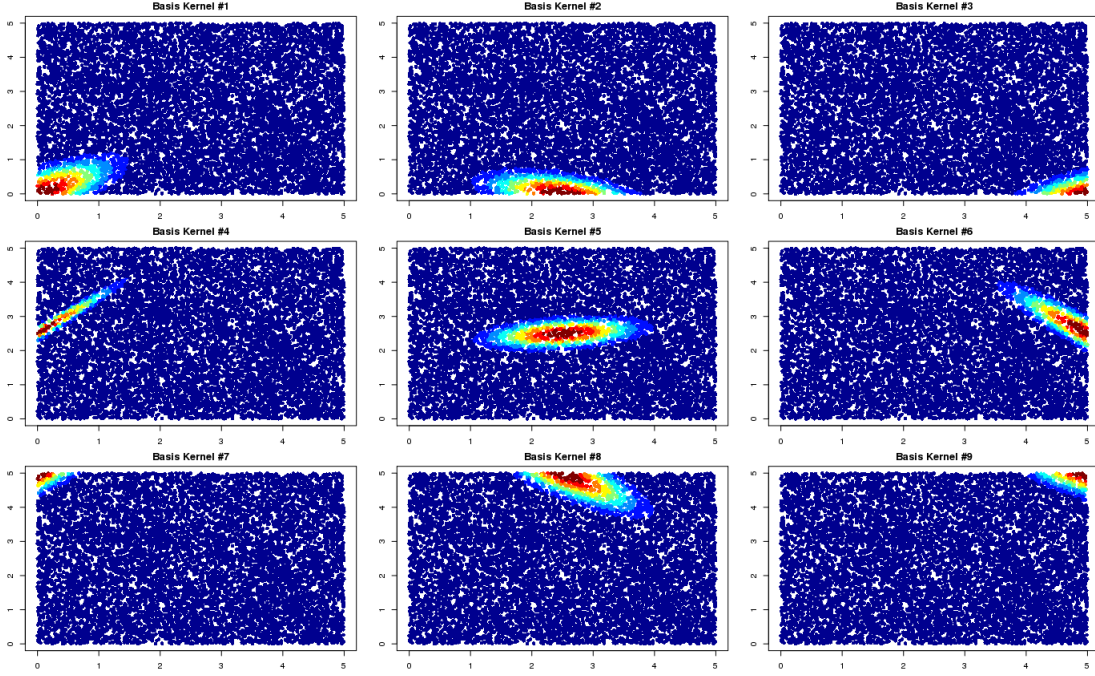
Figure 7: "Basis" Kernel functions $K_m(\cdot)$ for locations b_m, $m = 1, ..., 9$.

follows:

$$\Sigma_1 = \begin{bmatrix} 0.50 & 0.30 \\ 0.30 & 0.33 \end{bmatrix} \qquad \Sigma_2 = \begin{bmatrix} 0.50 & -0.12 \\ -0.12 & 0.13 \end{bmatrix} \qquad \Sigma_3 = \begin{bmatrix} 0.50 & 0.18 \\ 0.18 & 0.20 \end{bmatrix}$$

$$\Sigma_4 = \begin{bmatrix} 0.50 & 0.54 \\ 0.54 & 0.60 \end{bmatrix} \qquad \Sigma_5 = \begin{bmatrix} 0.50 & 0.06 \\ 0.06 & 0.07 \end{bmatrix} \qquad \Sigma_6 = \begin{bmatrix} 0.50 & -0.48 \\ -0.48 & 0.53 \end{bmatrix}$$

$$\Sigma_7 = \begin{bmatrix} 0.50 & 0.42 \\ 0.42 & 0.46 \end{bmatrix} \qquad \Sigma_8 = \begin{bmatrix} 0.50 & -0.36 \\ -0.36 & 0.40 \end{bmatrix} \qquad \Sigma_9 = \begin{bmatrix} 0.50 & -0.24 \\ -0.24 & 0.26 \end{bmatrix}$$
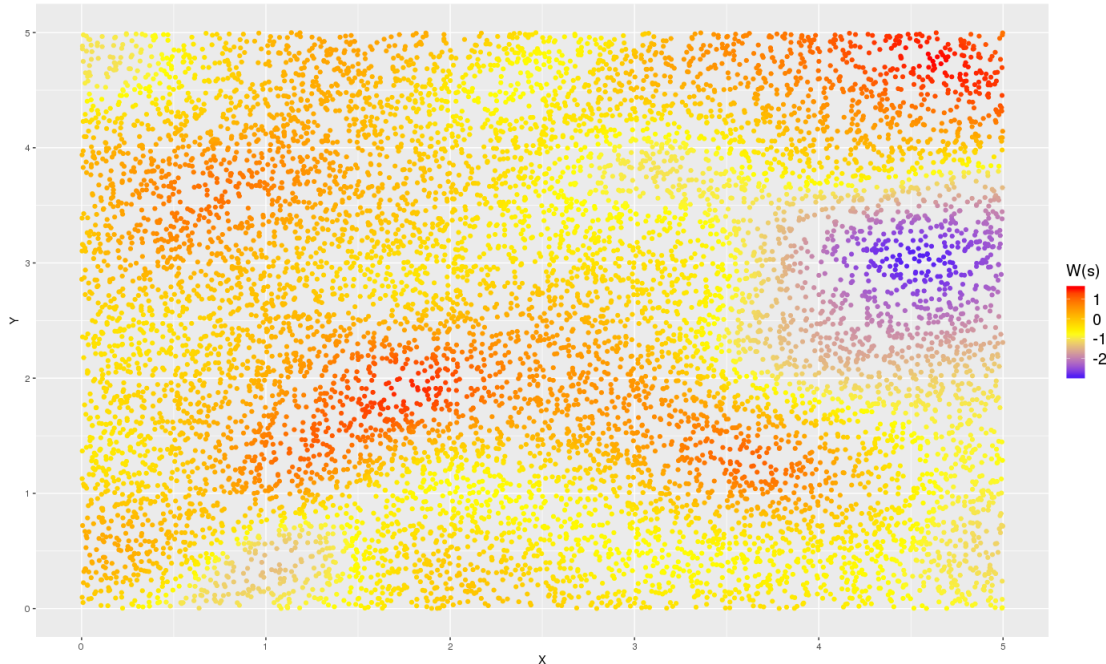
Figure 8: Nonstationary spatial random field constructed via convolutions of Gaussian basis kernels.

C Computing weights via parallelization

As mentioned in Section 3.1 (step 4), we propose a parallelized method to compute weights $c_k(\mathbf{s})$ for $k = 1, ..., K$ and $\mathbf{s} \in \mathcal{S}$. For a given location $\mathbf{s}$, the weights $c_k(\mathbf{s}) \propto \exp\left(-\|\mathbf{s} - \widetilde{\mathbf{s}}_k\|^2\right)$ where $\widetilde{\mathbf{s}}_k \in \mathcal{S}_k$ is the point in partition k with the shortest distance to point $\mathbf{s}$. The challenge lies in computing and storing the distances $\|\mathbf{s} - \widetilde{\mathbf{s}}_k\|$. Naive implementations may simply compute the distance matrix between all N locations, which requires $\mathcal{O}(n^2)$ operations as well as $\mathcal{O}(n^2)$ in storage. In the MODIS example (Section 5.2), the distance matrix ($n = 1$million observations) demands $8TB$ of storage.

We propose "streaming" the weight calculations ($c_k(\mathbf{s})$) without storing the distance matrix. First, we parallelize over C available cores where each core is assigned a location $\boldsymbol{s}$. Then, we compute distances between location $\boldsymbol{s}$ and the other locations $\boldsymbol{s}_-$. This

33
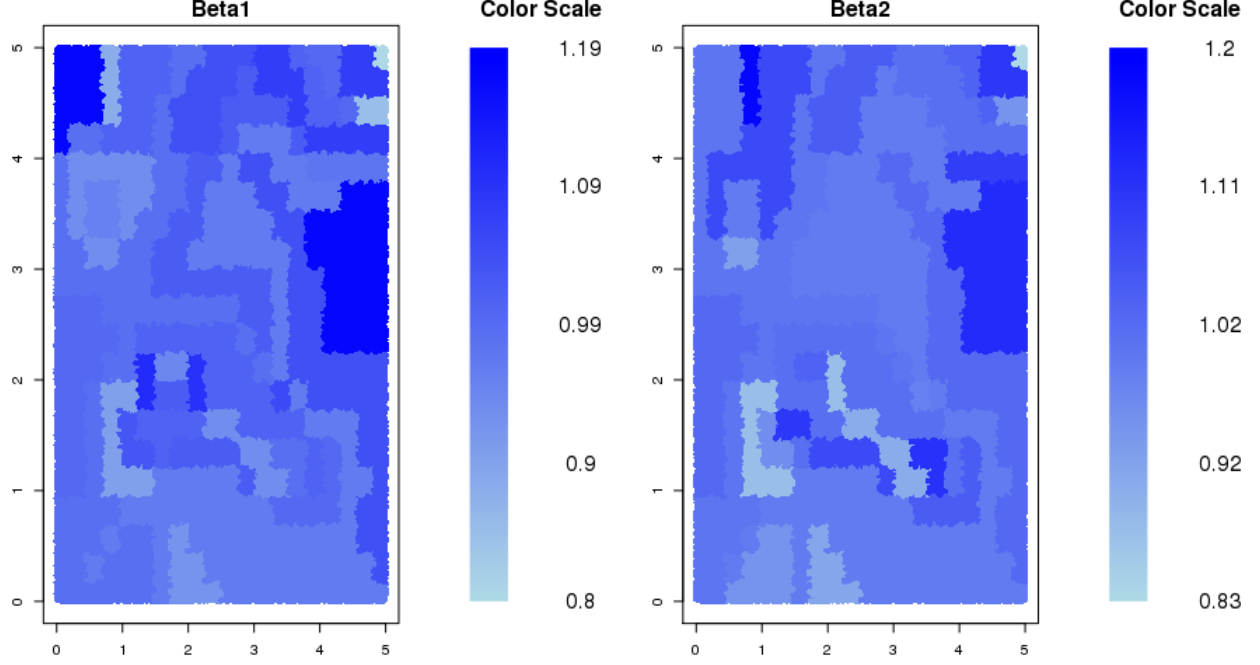
Figure 9: Map of the spatially-varying β_1 parameter (left) and β_2 parameter (right) for the simulated Poisson Dataset)

n-dimensional vector of distances (e.g. $8MB$ for the MODIS case) can be stored in the

random access memory (RAM). Finally, we compute the weights $c_k(\mathbf{s})$ for each partition k.

The task concludes once $c_k(\mathbf{s})$ are computed for all $\boldsymbol{s}$ in our dataset and for all partitions

k.
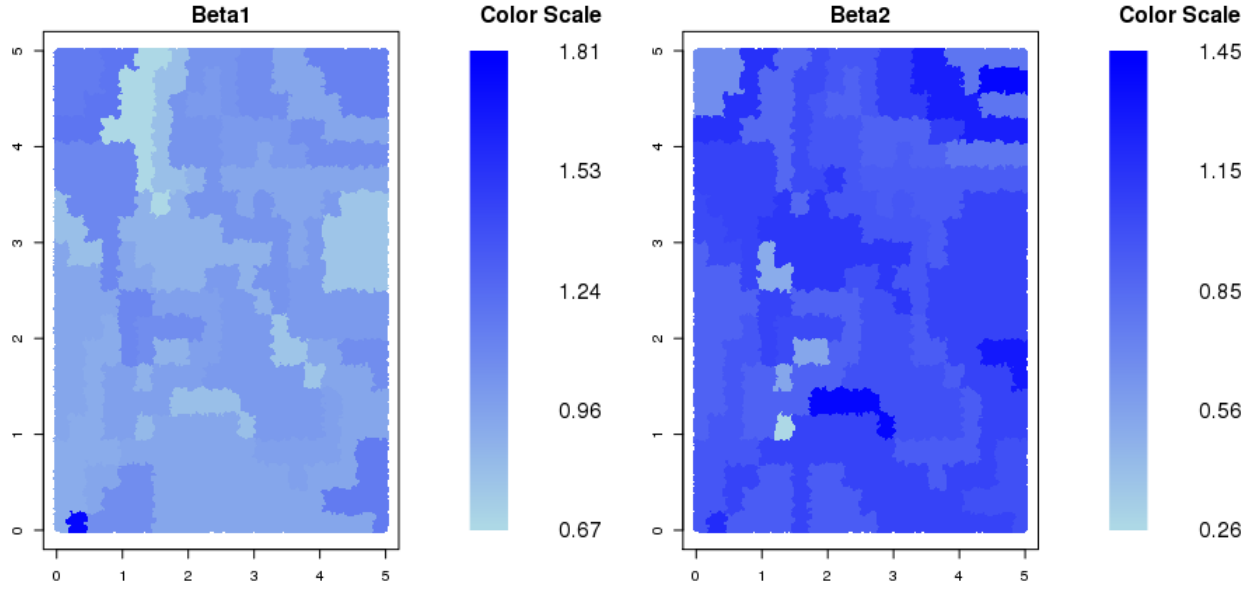
D   Partition Varying Estimates

Figure 10: Map of the spatially-varying β_1 parameter (left) and β_2 parameter (right) for the simulated Binary Dataset)
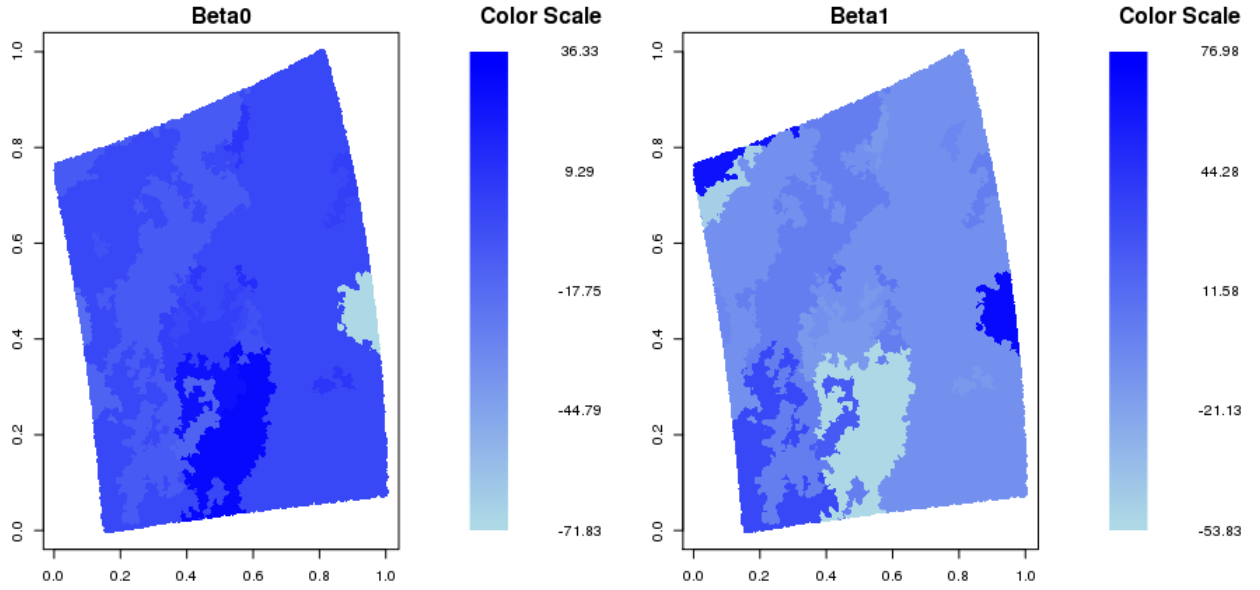

Figure 11: Map of the spatially-varying β_0 parameter (left) and β_1 parameter (right) for the MODIS cloud mask dataset.)

	Count Data		Binary Data	
Partition	β_1	β_2	β_1	β_2
1	0.93 (0.87,0.98)	0.98 (0.93,1.04)	0.99 (0.96,1.02)	1.02 (0.98,1.05)
2	1.02 (0.92,1.13)	0.98 (0.87,1.08)	1.01 (0.98,1.06)	1 (0.96,1.04)
3	0.95 (0.72,1.18)	1.08 (0.86,1.31)	1.03 (0.96,1.1)	1 (0.94,1.07)
4	1.03 (0.81,1.24)	1.15 (0.95,1.37)	1 (0.93,1.08)	1.05 (0.98,1.12)

Table 6: For $K = 4$ partitions, we report parameter estimates for β_1 and β_2 for the simulated count and binary datasets. This includes the posterior mean and 95% credible intervals for each partition.

	Count Data		Binary Data	
Partition	β_1	β_2	β_1	β_2
1	0.91 (0.77,1.06)	0.97 (0.83,1.11)	0.99 (0.94,1.03)	1.01 (0.97,1.06)
2	0.97 (0.88,1.05)	1.03 (0.95,1.12)	1 (0.95,1.05)	1 (0.95,1.05)
3	0.94 (0.64,1.25)	0.96 (0.65,1.28)	1.08 (0.97,1.2)	1.05 (0.94,1.17)
4	1 (0.7,1.31)	0.95 (0.65,1.24)	0.97 (0.87,1.08)	0.97 (0.86,1.08)
5	1.02 (0.92,1.12)	0.98 (0.87,1.08)	1.01 (0.95,1.07)	1.03 (0.97,1.09)
6	0.95 (0.72,1.17)	1.08 (0.86,1.31)	1.03 (0.96,1.1)	1 (0.93,1.07)
7	0.94 (0.84,1.03)	1.02 (0.92,1.12)	0.94 (0.86,1.02)	1.05 (0.96,1.13)
8	1.03 (0.82,1.24)	1.15 (0.95,1.37)	1.06 (0.98,1.15)	1.02 (0.93,1.11)
9	1.16 (0.79,1.54)	0.69 (0.31,1.05)	1 (0.93,1.07)	1.05 (0.97,1.12)

Table 7: For $K = 9$ partitions, we report parameter estimates for β_1 and β_2 for the simulated count and binary datasets. This includes the posterior mean and 95% credible intervals for each partition.

	Count Data		Binary Data	
Partition	β_1	β_2	β_1	β_2
1	0.94 (0.72,1.15)	1 (0.79,1.22)	0.99 (0.93,1.04)	1.03 (0.97,1.08)
2	1.06 (0.7,1.41)	0.95 (0.58,1.3)	1 (0.95,1.05)	0.99 (0.95,1.04)
3	0.98 (0.89,1.07)	1.02 (0.93,1.11)	1.08 (0.97,1.19)	1.06 (0.95,1.17)
4	0.93 (0.62,1.24)	0.98 (0.66,1.28)	0.97 (0.86,1.08)	0.97 (0.86,1.08)
5	0.99 (0.69,1.29)	0.95 (0.67,1.26)	1 (0.88,1.12)	1.03 (0.91,1.15)
6	0.91 (0.72,1.11)	0.94 (0.75,1.14)	0.91 (0.78,1.04)	0.87 (0.75,1)
7	1.02 (0.92,1.13)	0.98 (0.87,1.09)	1 (0.85,1.15)	1.12 (0.97,1.27)
8	0.83 (0.44,1.21)	1.44 (1.02,1.82)	1.02 (0.95,1.08)	1.02 (0.95,1.09)
9	1.02 (0.66,1.35)	0.91 (0.56,1.27)	1.03 (0.95,1.11)	1 (0.93,1.08)
10	1.02 (0.75,1.29)	1.08 (0.81,1.35)	1.03 (0.88,1.18)	1.02 (0.88,1.17)
11	0.98 (0.86,1.1)	1.03 (0.91,1.15)	0.94 (0.86,1.03)	1.05 (0.96,1.13)
12	0.79 (0.4,1.21)	1.1 (0.68,1.51)	1.18 (0.97,1.39)	1 (0.8,1.21)
13	0.86 (0.69,1.03)	1 (0.84,1.18)	1.08 (0.97,1.19)	1.02 (0.91,1.13)
14	0.96 (0.69,1.23)	1.29 (1.02,1.57)	1.02 (0.87,1.16)	1.02 (0.87,1.17)
15	1.16 (0.78,1.54)	0.69 (0.31,1.05)	0.95 (0.85,1.06)	1.02 (0.91,1.12)
16	1.13 (0.79,1.47)	0.96 (0.63,1.29)	1.05 (0.96,1.15)	1.09 (0.99,1.18)

Table 8: For $K = 16$ partitions, we report parameter estimates for β_1 and β_2 for the simulated count and binary datasets. This includes the posterior mean and 95% credible intervals for each partition.

	Count Data		Binary Data	
Partition	β_1	β_2	β_1	β_2
1	0.94 (0.72,1.15)	1.01 (0.79,1.22)	0.99 (0.94,1.05)	1.03 (0.97,1.08)
2	1.07 (0.72,1.43)	0.95 (0.59,1.32)	0.99 (0.74,1.23)	0.95 (0.69,1.2)
3	0.96 (0.83,1.08)	1.08 (0.95,1.21)	1 (0.96,1.05)	1 (0.96,1.06)
4	0.94 (0.63,1.25)	0.96 (0.65,1.28)	0.93 (0.75,1.12)	0.92 (0.73,1.11)
5	1.19 (0.85,1.52)	1.03 (0.68,1.35)	1.06 (0.93,1.19)	1.03 (0.9,1.16)
6	1 (0.7,1.3)	0.95 (0.65,1.25)	0.97 (0.86,1.08)	0.97 (0.86,1.07)
7	0.91 (0.71,1.1)	0.94 (0.75,1.14)	1 (0.88,1.11)	1.03 (0.91,1.14)
8	1.05 (0.91,1.19)	0.98 (0.84,1.11)	0.91 (0.78,1.03)	0.87 (0.75,1)
9	0.83 (0.44,1.21)	1.44 (1.05,1.85)	1 (0.85,1.14)	1.12 (0.97,1.27)
10	1.02 (0.8,1.25)	1.03 (0.8,1.26)	1.02 (0.94,1.08)	1.02 (0.95,1.09)
11	1.01 (0.73,1.3)	1.02 (0.72,1.29)	1.04 (0.88,1.2)	0.96 (0.81,1.11)
12	1.01 (0.67,1.36)	0.92 (0.56,1.26)	1.02 (0.85,1.18)	1.11 (0.94,1.27)
13	0.79 (0.36,1.23)	0.96 (0.54,1.41)	1.11 (0.91,1.31)	1.01 (0.81,1.21)
14	1.08 (0.55,1.59)	1.33 (0.82,1.86)	1.03 (0.88,1.18)	1.02 (0.87,1.16)
15	1.03 (0.75,1.29)	1.08 (0.8,1.35)	1.01 (0.89,1.14)	0.96 (0.84,1.08)
16	0.98 (0.86,1.11)	1.03 (0.91,1.15)	1.19 (0.95,1.42)	1.14 (0.9,1.38)
17	1.06 (0.8,1.32)	0.97 (0.71,1.23)	0.93 (0.7,1.16)	0.93 (0.69,1.16)
18	0.79 (0.37,1.19)	1.09 (0.68,1.5)	0.93 (0.84,1.03)	1.08 (0.98,1.18)
19	0.96 (0.73,1.2)	0.96 (0.72,1.2)	0.96 (0.82,1.1)	0.99 (0.85,1.13)
20	0.73 (0.53,0.93)	0.94 (0.75,1.13)	1.15 (0.95,1.37)	1.01 (0.8,1.21)
21	1.01 (0.74,1.29)	0.94 (0.66,1.21)	1.08 (0.97,1.19)	1.02 (0.91,1.13)
22	1.21 (0.87,1.53)	1.21 (0.89,1.53)	1.02 (0.87,1.16)	1.02 (0.87,1.17)
23	0.96 (0.7,1.23)	1.29 (1.02,1.56)	0.95 (0.84,1.06)	1.01 (0.91,1.12)
24	1.16 (0.79,1.55)	0.69 (0.33,1.06)	1.08 (0.98,1.18)	1.11 (1.01,1.2)
25	1.14 (0.8,1.47)	0.96 (0.63,1.29)	0.8 (0.46,1.13)	0.83 (0.47,1.19)

Table 9: For $K = 25$ partitions, we report parameter estimates for β_1 and β_2 for the simulated count and binary datasets. This includes the posterior mean and 95% credible intervals for each partition.

Partition	Count Data β_1	Count Data β_2	Binary Data β_1	Binary Data β_2
1	0.91 (0.68,1.12)	0.99 (0.77,1.21)	0.99 (0.94,1.05)	1.01 (0.95,1.06)
2	1.81 (0.68,2.88)	1.22 (0.15,2.28)	0.99 (0.74,1.24)	0.95 (0.69,1.2)
3	1.07 (0.71,1.43)	0.95 (0.58,1.3)	0.98 (0.9,1.06)	1 (0.92,1.08)
4	0.95 (0.83,1.08)	1.08 (0.95,1.21)	0.93 (0.74,1.12)	0.91 (0.72,1.11)
5	0.94 (0.64,1.25)	0.96 (0.64,1.27)	1.05 (0.93,1.19)	1.03 (0.91,1.16)
6	1.19 (0.85,1.53)	1.03 (0.68,1.36)	1 (0.84,1.17)	1.04 (0.88,1.2)
7	1 (0.69,1.29)	0.95 (0.65,1.24)	1 (0.88,1.11)	1.03 (0.91,1.15)
8	0.94 (0.72,1.16)	0.92 (0.7,1.14)	0.91 (0.78,1.03)	0.87 (0.75,1)
9	0.99 (0.77,1.2)	0.91 (0.7,1.12)	1.03 (0.82,1.22)	1.08 (0.87,1.28)
10	0.84 (-0.08,1.73)	0.26 (-0.59,1.15)	0.94 (0.8,1.09)	0.91 (0.77,1.06)
11	0.83 (0.45,1.23)	1.45 (1.05,1.85)	1 (0.85,1.15)	1.12 (0.97,1.27)
12	1.02 (0.8,1.25)	1.03 (0.8,1.25)	1.02 (0.94,1.08)	1.02 (0.95,1.09)
13	1.01 (0.72,1.29)	1.02 (0.73,1.3)	1.04 (0.88,1.19)	0.96 (0.81,1.12)
14	0.89 (0.27,1.48)	0.54 (-0.04,1.17)	1.01 (0.84,1.18)	1.11 (0.94,1.28)
15	0.79 (0.35,1.24)	0.97 (0.54,1.41)	0.97 (0.87,1.08)	1 (0.89,1.1)
16	1.09 (0.54,1.59)	1.32 (0.81,1.86)	1.12 (0.92,1.32)	1.01 (0.82,1.21)
17	1.12 (0.94,1.32)	1.1 (0.91,1.3)	1.03 (0.88,1.18)	1.02 (0.87,1.17)
18	1.08 (0.65,1.5)	1.06 (0.63,1.5)	1.1 (0.91,1.28)	0.87 (0.7,1.05)
19	1.02 (0.76,1.29)	1.08 (0.81,1.35)	1.06 (0.67,1.46)	0.98 (0.57,1.39)
20	0.9 (0.72,1.09)	1.17 (0.99,1.36)	0.95 (0.78,1.11)	1.04 (0.87,1.2)
21	1.06 (0.8,1.32)	0.97 (0.72,1.24)	1.02 (0.92,1.12)	0.99 (0.89,1.09)
22	0.96 (0.48,1.48)	0.52 (0.03,1.03)	1.19 (0.95,1.42)	1.13 (0.9,1.38)
23	0.79 (0.38,1.2)	1.1 (0.67,1.51)	0.94 (0.71,1.18)	0.93 (0.7,1.15)
24	0.83 (0.41,1.26)	1.06 (0.64,1.51)	0.93 (0.84,1.03)	1.08 (0.98,1.18)
25	0.96 (0.72,1.2)	0.96 (0.72,1.2)	0.96 (0.82,1.1)	0.99 (0.86,1.13)
26	0.67 (0.42,0.92)	0.88 (0.62,1.13)	0.98 (0.78,1.19)	1.1 (0.89,1.31)
27	0.82 (0.52,1.16)	1.04 (0.72,1.35)	1.18 (0.97,1.39)	1 (0.79,1.2)
28	1.04 (0.79,1.28)	0.99 (0.76,1.25)	1.02 (0.9,1.13)	1.08 (0.96,1.19)
29	1.01 (0.75,1.29)	0.94 (0.66,1.2)	1.05 (0.89,1.22)	1.04 (0.88,1.2)
30	1.07 (0.66,1.47)	0.81 (0.4,1.21)	1.08 (0.97,1.19)	1.02 (0.91,1.13)
31	1.21 (0.89,1.54)	1.19 (0.88,1.53)	0.89 (0.62,1.14)	1.2 (0.95,1.47)
32	1.08 (0.77,1.38)	1.11 (0.81,1.42)	1.02 (0.87,1.16)	1.02 (0.87,1.17)
33	0.97 (0.69,1.23)	1.29 (1.01,1.56)	1 (0.87,1.13)	1.04 (0.91,1.18)
34	1.16 (0.79,1.55)	0.68 (0.31,1.05)	0.85 (0.66,1.03)	0.96 (0.78,1.13)
35	1.14 (0.76,1.52)	0.82 (0.44,1.19)	1.08 (0.98,1.18)	1.11 (1.01,1.2)
36	1.13 (0.45,1.88)	1.42 (0.74,2.13)	0.8 (0.48,1.14)	0.83 (0.47,1.18)

Table 10: For $K = 36$ partitions, we report parameter estimates for β_1 and β_2 for the simulated count and binary datasets. This includes the posterior mean and 95% credible intervals for each partition.

References

Banerjee, A., Dunson, D. B., and Tokdar, S. T. (2013). Efficient Gaussian process regression for large datasets. *Biometrika*, 100(1):75–89.

Banerjee, S. and Gelfand, A. E. (2006). Bayesian wombling: Curvilinear gradient assessment under spatial process models. *Journal of the American Statistical Association*, 101(476):1487–1501.

Banerjee, S., Gelfand, A. E., Finley, A. O., and Sang, H. (2008). Gaussian predictive process models for large spatial data sets. *Journal of the Royal Statistical Society: Series B (Statistical Methodology)*, 70(4):825–848.

Bradley, J. R., Cressie, N., Shi, T., et al. (2016). A comparison of spatial predictors when datasets could be very large. *Statistics Surveys*, 10:100–131.

Bradley, J. R., Holan, S. H., and Wikle, C. K. (2019). Bayesian hierarchical models with conjugate full-conditional distributions for dependent data from the natural exponential family. *Journal of the American Statistical Association*, 0(ja):1–29.

Christensen, O. F., Roberts, G. O., and Sköld, M. (2006). Robust Markov chain Monte Carlo methods for spatial generalized linear mixed models. *Journal of Computational and Graphical Statistics*, 15(1):1–17.

Cressie, N. (2015). *Statistics for spatial data.* John Wiley & Sons.

Cressie, N. and Johannesson, G. (2008). Fixed rank kriging for very large spatial data sets.

Journal of the Royal Statistical Society: Series B (Statistical Methodology), 70(1):209–226.

de Valpine, P., Turek, D., Paciorek, C., Anderson-Bergman, C., Temple Lang, D., and Bodik, R. (2017). Programming with models: writing statistical algorithms for general model structures with NIMBLE. *Journal of Computational and Graphical Statistics*, 26:403–413.

Diggle, P. J., Tawn, J., and Moyeed, R. (1998). Model-based geostatistics. *Journal of the Royal Statistical Society: Series C (Applied Statistics)*, 47(3):299–350.

Ejigu, B. A., Wencheko, E., Moraga, P., and Giorgi, E. (2020). Geostatistical methods for modelling non-stationary patterns in disease risk. *Spatial Statistics*, 35:100397.

Friedman, J., Hastie, T., and Tibshirani, R. (2010a). Regularization paths for generalized linear models via coordinate descent. *Journal of statistical software*, 33(1):1.

Friedman, J., Hastie, T., and Tibshirani, R. (2010b). Regularization paths for generalized linear models via coordinate descent. *Journal of Statistical Software*, 33(1):1–22.

Fuentes, M. (2001). A high frequency kriging approach for non-stationary environmental processes. *Environmetrics: The official journal of the International Environmetrics Society*, 12(5):469–483.

Fuentes, M. (2002). Interpolation of nonstationary air pollution processes: a spatial spectral approach. *Statistical Modelling*, 2(4):281–298.

Gopal, S., Ma, Y., Xin, C., Pitts, J., and Were, L. (2019). Characterizing the spatial determinants and prevention of malaria in Kenya. *International journal of environmental research and public health*, 16(24):5078.

Griffith, D. A. (2003). Spatial filtering. In *Spatial Autocorrelation and Spatial Filtering*, pages 91–130. Springer.

Guan, Y. and Haran, M. (2018). A computationally efficient projection-based approach for spatial generalized linear mixed models. *Journal of Computational and Graphical Statistics*, 27(4):701–714.

Guhaniyogi, R. and Banerjee, S. (2018). Meta-kriging: Scalable Bayesian modeling and inference for massive spatial datasets. *Technometrics*, 60(4):430–444.

Haran, M., Hodges, J. S., and Carlin, B. P. (2003). Accelerating computation in markov random field models for spatial data via structured mcmc. *Journal of Computational and Graphical Statistics*, 12(2):249–264.

Heaton, M. J., Christensen, W. F., and Terres, M. A. (2017). Nonstationary gaussian process models using spatial hierarchical clustering from finite differences. *Technometrics*, 59(1):93–101.

Hefley, T. J., Broms, K. M., Brost, B. M., Buderman, F. E., Kay, S. L., Scharf, H. R., Tipton, J. R., Williams, P. J., and Hooten, M. B. (2017). The basis function approach for modeling autocorrelation in ecological data. *Ecology*, 98(3):632–646.

Higdon, D. (1998). A process-convolution approach to modelling temperatures in the North
Atlantic Ocean. *Environmental and Ecological Statistics*, 5(2):173–190.

Higdon, D., Gattiker, J., Williams, B., and Rightley, M. (2008). Computer model cali-
bration using high-dimensional output. *Journal of the American Statistical Association*,
103(482):570–583.

Holland, D. M., Saltzman, N., Cox, L. H., and Nychka, D. (1999). Spatial prediction of sul-
fur dioxide in the eastern United States. In *geoENV II—Geostatistics for environmental
applications*, pages 65–76. Springer.

Hughes, J. and Haran, M. (2013). Dimension reduction and alleviation of confounding for
spatial generalized linear mixed models. *Journal of the Royal Statistical Society: Series
B (Statistical Methodology)*, 75(1):139–159.

ICF (2004-2017 (Accessed July, 1, 2020)). Demographic and health surveys (various)
[datasets]. Funded by USAID. Data retrieved from , `http://dhsprogram.com/data/`
`available-datasets.cfm`.

Katzfuss, M. (2013). Bayesian nonstationary spatial modeling for very large datasets.
Environmetrics, 24(3):189–200.

Katzfuss, M. (2017). A multi-resolution approximation for massive spatial datasets. *Journal
of the American Statistical Association*, 112(517):201–214.

Kim, H.-M., Mallick, B. K., and Holmes, C. (2005). Analyzing nonstationary spatial data

using piecewise gaussian processes. *Journal of the American Statistical Association*, 100(470):653–668.

Kleiber, W. and Nychka, D. (2012). Nonstationary modeling for multivariate spatial processes. *Journal of Multivariate Analysis*, 112:76–91.

Lee, B. S. and Haran, M. (2019). Picar: An efficient extendable approach for fitting hierarchical spatial models. *arXiv preprint arXiv:1912.02382*.

Minsker, S., Srivastava, S., Lin, L., and Dunson, D. B. (2017). Robust and scalable Bayes via a median of subset posterior measures. *The Journal of Machine Learning Research*, 18(1):4488–4527.

Nychka, D., Bandyopadhyay, S., Hammerling, D., Lindgren, F., and Sain, S. (2015). A multiresolution Gaussian process model for the analysis of large spatial datasets. *Journal of Computational and Graphical Statistics*, 24(2):579–599.

Nychka, D., Wikle, C., and Royle, J. A. (2002). Multiresolution models for nonstationary spatial covariance functions. *Statistical Modelling*, 2(4):315–331.

O'Hara, R. B., Sillanpää, M. J., et al. (2009). A review of Bayesian variable selection methods: what, how and which. *Bayesian analysis*, 4(1):85–117.

Paciorek, C. J. and Schervish, M. J. (2006). Spatial modelling using a new class of nonstationary covariance functions. *Environmetrics: The official journal of the International Environmetrics Society*, 17(5):483–506.

Risser, M. D. and Calder, C. A. (2015). Local likelihood estimation for covariance functions with spatially-varying parameters: the convospat package for r. *arXiv preprint arXiv:1507.08613*.

Royle, J. A. and Wikle, C. K. (2005). Efficient statistical mapping of avian count data. *Environmental and Ecological Statistics*, 12(2):225–243.

Rue, H., Martino, S., and Chopin, N. (2009). Approximate bayesian inference for latent gaussian models by using integrated nested laplace approximations. *Journal of the royal statistical society: Series b (statistical methodology)*, 71(2):319–392.

Sampson, P. (2010). Constructions for nonstationary spatial processes in gelfand ae, diggle pj, fuentes m, and guttorp p (ed.), the handbook of spatial statistics, chapter 9.

Scott, S. L., Blocker, A. W., Bonassi, F. V., Chipman, H. A., George, E. I., and McCulloch, R. E. (2016). Bayes and big data: The consensus Monte Carlo algorithm. *International Journal of Management Science and Engineering Management*, 11(2):78–88.

Sengupta, A. and Cressie, N. (2013). Hierarchical statistical modeling of big spatial datasets using the exponential family of distributions. *Spatial Statistics*, 4:14–44.

Shaby, B. and Wells, M. T. (2010). Exploring an adaptive metropolis algorithm. *Currently under review*, 1(1):17.

Shi, T. and Cressie, N. (2007). Global statistical analysis of misr aerosol data: a massive data product from nasa's terra satellite. *Environmetrics: The official journal of the International Environmetrics Society*, 18(7):665–680.

Tibshirani, R. (1996). Regression shrinkage and selection via the lasso. *Journal of the Royal Statistical Society: Series B (Methodological)*, 58(1):267–288.

Zilber, D. and Katzfuss, M. (2020). Vecchia-Laplace approximations of generalized Gaussian processes for big non-Gaussian spatial data. *Computational Statistics & Data Analysis*, page 107081.